Nanoscale

PAPER

View Article Online
View Journal | View Issue

Cite this: *Nanoscale*, 2024, **16**, 5574

A sensitive lateral flow test strip sensor for visual detection of acid red 18 in food using bicentric-emission carbon dots†

Houwen Hu,‡[a] Zewei Chen,‡[b] Tingting Li,[a] Linfan Wang,[a] Haoming Xing,[a] Guoqiang Guo,[a,c] Gang Wang *[a,d] and Da Chen *[a]

Hazardous synthetic colorants have found widespread use in food production, and excessive consumption of these pigments can pose potential risks to human health. In this study, we propose an ultrasensitive fluorescence method for the analysis of Acid Red 18 (AR18) in food products. The method is based on the nitrogen-doped carbon dots (N-CDs) derived from tris and resorcinol through a hydrothermal way. The as-synthesized N-CDs exhibit two emission centers at 425 nm and 541 nm, corresponding to the excitation wavelengths of 377 nm and 465 nm, respectively. Upon the addition of AR18, the fluorescence intensity at 541 nm significantly decreases with a simultaneous, though less pronounced, reduction in the intensity at 425 nm, which is attributed to the localization of fluorescence resonance energy transfer (L-FRET). Specifically, a novel ratiometric fluorescent probe was constructed based on the extracted data from the 3D fluorescence excitation–emission matrix. This probe demonstrates a wide linear range from 0.0539 to 30 μM and a low limit of detection (LOD) of 53.9 nM. For practical applications, a portable fluorescent sensor based on a lateral flow test strip (LFTS) was designed for real-time monitoring of AR18. Color channel values were determined using a smartphone application, resulting in a satisfactory LOD of 75.3 nM. Furthermore, the suitability of the proposed ratiometric fluorescent probe was validated through the detection of AR18 in real food samples, consistently achieving recovery rates in the range of 99.7–101.4%. This research not only expands the scope of CDs in sensing fields, but also provides an effective strategy for the development of an excellent platform for real-time AR18 detection, contributing to public food safety.

Received 8th November 2023,
Accepted 1st February 2024

DOI: 10.1039/d3nr05662g

rsc.li/nanoscale

1. Introduction

Food colorants, considered essential food additives, are widely employed in food preparation to enhance product aesthetics and appeal to consumers. They are used in various food and beverage products, including drinks, desserts, sauces and culinary items.[1] These colorants can be derived from natural sources or synthesized using chemical methods. While natural colorants obtained directly from plant and animal tissues are generally considered safe for human consumption, they often exhibit poor resistance to factors such as light, heat, and chemical reactions.[2] Recently, synthetic pigments have gained popularity in the food industry due to their vibrant color, strong coloring capabilities, stability, and cost-effectiveness. Among these synthetic colorants, AR18, classified as an azo dye, is one of the most commonly used dyes in food products, contributing to their vivid reddish appearance.[3,4] However, an excessive consumption of AR18 can pose health risks to individuals, primarily due to the presence of an azo group and aromatic ring structures within AR18. Studies have revealed that the decomposition of azo compounds in the body can lead to the formation of two aromatic amines upon interacting with target cells after metabolic activities, which can potentially increase the risk of cancer.[5,6] Besides, over-consumption of AR18 may disrupt normal metabolic function in the body, leading to hyperactivity in children and allergic reactions in adults.[7] Presently, analytical methods used to detect AR18 levels, such as high-performance liquid chromatography

[a]*Department of Microelectronic Science and Engineering, School of Physical Science and Technology, Ningbo University, Ningbo 315211, P. R. China.*
E-mail: gangwang@nbu.edu.cn, chenda@nbu.edu.cn
[b]*Department of Electrical and Electronic Engineering, Synchrotron Light Application Center, Saga University, Saga 840-8502, Japan*
[c]*Department of Materials Science and Engineering, Shenzhen Key Laboratory of Full Spectral Solar Electricity Generation (FSSEG), Southern University of Science and Technology, Shenzhen 518055, P. R. China*
[d]*National Key Laboratory of Materials for Integrated Circuits, Shanghai Institute of Microsystem and Information Technology, Chinese Academy of Sciences, Shanghai 200050, P. R. China*

†Electronic supplementary information (ESI) available: Fig. S1–S14. See DOI: https://doi.org/10.1039/d3nr05662g

‡These authors contributed equally to this work.

(HPLC),[8] electrochemical analysis,[9,10] and capillary electrophoresis,[11] suffer from inherent limitations. These drawbacks include the need for specialized equipment, skilled operations, time-consuming preparation, and high detection costs, which restrict their widespread applications. As a result, there is a pressing need to develop a simple, rapid and sensitive strategy for quantifying AR18 levels in food products.

In recent years, CDs, an emerging class of carbon-based luminescent nanomaterials, have attracted significant attention due to their exceptional properties, such as excellent solubility in water, ease of preparation, high stability, outstanding photostability, superior bio-compatibility, and low toxicity.[12–15] Notably, CDs have found widespread utility in various detection applications, primarily owing to their outstanding optical characteristics. Several fluorescent probes based on CDs have been developed for the detection of AR18. For instance, Liu *et al.* introduced an innovative AR18 detection based on the fluorescence quenching of N, P-doped CDs using AR18 through the inner filter effect (IFE).[4] Cui *et al.* established an efficient AR18 sensing system using orange-emissive CDs, relying on fluorescence quenching through the IFE.[16] However, most CD-based AR18 sensors employ a single-emission probe, making them susceptible to variations in instrumentation and environmental factors. Ratiometric fluorescent probes are increasingly gaining attention due to their unique capability to provide intrinsic self-calibration for signals. For example, Tu *et al*. developed a ratiometric fluorescence method using CDs derived from fangchinoline and o-phenylenediamine for sensitive and selective AR18 detection.[17] Nonetheless, these probes often rely on single-wavelength excitation, rendering them highly dependent on environmental conditions and susceptible to experimental errors. On the other hand, an overwhelming majority of fluorescent sensors stick to analysis based on emission signals generated by single-wavelength excitation, while analytical methods depending on emission signals at different excitation wavelengths have rarely been reported, which is inconducive to the diversity and innovativeness of sensors. Meanwhile, conventional fluorescence analysis methods are not conducive to real-time use, as they typically require trained professionals and specific laboratory conditions. This limitation significantly hinders the practical application of fluorescence sensing in real samples.[18] Hence, the development of a precise, sensitive and real-time fluorescence sensing platform for the determination of AR18 is of great significance.

In this study, N-CDs with bicentric fluorescence regions were synthesized *via* a straightforward one-step hydrothermal synthesis method using tris and resorcinol as precursors. The resulting N-CDs exhibit two distinct intrinsic fluorescence emission centers, emitting at 425 nm and 541 nm, with the corresponding excitation wavelengths of 377 nm and 465 nm, respectively. When AR18 is introduced, the two emission centers display varying degrees of quenching, primarily attributed to the localization of fluorescence resonance energy transfer (L-FRET). This phenomenon is a result of the accurate spectral overlap between the absorption of AR18 and the longer emission wavelength of N-CDs at 541 nm. Consequently, we establish a ratiometric fluorescent probe for the determination of AR18 based on the changes in bicentric emissions derived from a three-dimensional (3D) fluorescence excitation–emission matrix of N-CDs. This approach results in excellent linearity across a concentration range of 0.0539–30 μM and an impressive detection limit (LOD) of 53.9 nM. Leveraging the unique fluorescence properties of N-CDs, we constructed a dual-channel fluorescence analytical device employing a lateral flow test strip (LFTS) for real-time AR18 detection in food samples. The color channel values can be conveniently determined using a smartphone application. This portable sensing platform demonstrates precision and accuracy, with recovery rates falling within the range of 99.7–101.4%. These findings pave the way for a novel approach to monitor AR18 levels in food products.

Gang Wang

Gang Wang is a professor in the School of Physical Science and Technology at Ningbo University, China. He received his B.S. degree from Lanzhou University in 2011 and Ph.D. degree from Lanzhou University in 2016. In 2011–2016, he co-educated in the State Key Laboratory of Functional Materials for Informatics, Shanghai Institute of Microsystem and Information Technology, Chinese Academy of Sciences. He joined Ningbo University in 2016. Research in his laboratory currently includes the preparation and application of graphene quantum dots, graphene films and vertically aligned graphene arrays, thin-film photoelectric devices and device physics. As the first author/corresponding author in Nature Electronics, Nature Communications, Advanced Energy Materials, Advanced Functional Materials, Advanced Optical Materials, ACS Applied Materials & Interfaces, Journal of Materials Chemistry A/B/C, Applied Physics Letters, Langmuir *and other international academic journals, he has published more than 100 academic papers.*

2. Experimental section

2.1. Materials and reagents

In this work, all analytical reagents were procured from Aladdin (Shanghai, China), including KCl, LiCl, AgCl, $BaCl_2$, $CoCl_2$, $MgCl_2$, $CdCl_2$, $FeCl_2$, alanine (Ala), l-asparagine (Asn), l-cysteine (Cys), glutathione (Glu), proline (Pro), serine (Ser), curcumin (Cur), tartrazine (Tar), sunset yellow (SY), amaranth red (AMR), AR18, tris, resorcinol, and other necessary chemicals. These reagents were utilized without the need for additional purification. For the preparation of reagents, ultra-

pure deionized water with a resistivity of 18.25 MΩ cm, sourced from Millipore, was employed throughout the experimental procedures.

2.2. Synthesis of N-CDs

N-CDs were synthesized *via* a straightforward hydrothermal reaction, employing tris and resorcinol as the carbon precursors (Fig. 1a). To begin, 2 mmol tris and 2 mmol resorcinol were combined in 20 mL of deionized water. The resulting solution was subjected to ultrasonic treatment for 10 minutes to ensure thorough dissolution. Following complete dissolution, the solution was transferred into a 100 mL Teflon reaction vessel and heated at 160 °C for 6 h. After naturally cooling, the obtained product was filtered using a 0.22 μm microporous syringe filter and subsequently dialyzed at room temperature for 24 hours utilizing a dialysis membrane with a molecular weight cutoff of 500 Da to obtain pure N-CDs. The obtained N-CDs were stored at 4 °C for subsequent experiments.

2.3. Instruments and measurements

Morphological and structural studies were conducted using transmission electron microscopy (TEM, JEM-2100F, Japan Electron) and atomic force microscopy (AFM, Cypher S, Oxford Instruments). FT-IR spectra were obtained using a Thermo Scientific Nicolet 6700 FT-IR spectrometer from 500–4000 cm^{-1}. XPS analysis was performed using an Axis Ultra DLD X-ray photoelectron spectrometer. The X-ray diffraction (XRD) spectrum and the Raman spectrum were recorded using an X-ray diffraction (PANalytical X'Pert Pro MPD) and a HORIBA Jobin Yvon HR800 Evolution. Fluorescence measurements were carried out using a PerkinElmer LS55 luminescence spectrometer (PerkinElmer Instruments, U.K.) at room temperature. UV-vis absorption spectra were recorded using a UV-5800 spectrophotometer.

2.4. Calculation equation of quantum yield (QY)

Rhodamine B was dissolved in absolute ethanol (refractive index η = 1.096, 25 °C) and employed as a reference. To minimize the self-absorption effect, the absorbance of both the reference sample solution and N-CD suspensions were controlled below 0.1 by dilution at the optimum excitation wavelength. The relative *QY* can be calculated using the following equation:

$$QY = QY_R\left(\frac{I_T A_R}{A_T I_R}\right) \times \left(\frac{\eta_T}{\eta_R}\right)^2 \quad (1)$$

where I represents the integrated fluorescence intensity, η is the refractive index of the solvent, and A refers to the absorbance at the optimum excitation wavelength. The subscript "R" and "T" refers to rhodamine B and N-CDs, respectively. For all these solutions, η_T/η_R is approximately equal to 1.

2.5. Fluorescence determination of AR18

In the fluorescence measurements, a range of AR18 solutions with known concentrations were added to 1.5 mL of N-CD solution, and the final total volume was maintained at 3 mL. After incubating the mixed solutions for 1 min, their fluorescence excitation–emission matrices were recorded at room temperature. Moreover, the effects of potential interferents on fluorescence intensities were evaluated to confirm the selectivity of N-CDs for AR18 detection. Each potential coexisting substance (at a concentration of 100 μM), which included amino acids, cations, and different food colorants, was mixed with the N-CD solution in a 1 : 1 volume ratio and transferred to a quartz cuvette. The fluorescence excitation–emission matrices of these samples were recorded using the same test

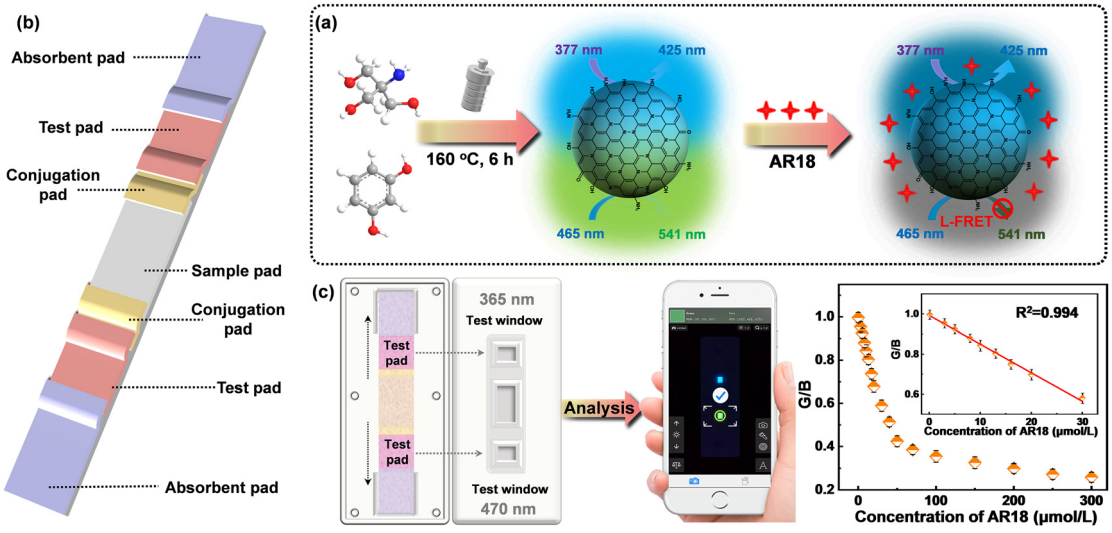

Fig. 1 Schematic representation of the preparation process and applications of N-CDs. (a) Schematic diagram of the preparation process of N-CDs. (b) Structure diagram of the LFTS. (c) Hardware design of a smartphone fluorometric sensing platform for AR18 detection using a smartphone app.

procedure as described above. In addition, the anti-interference ability of the proposed method for AR18 detection was examined in the presence of each interferent and the concentration of each substance in a solution was 100 μM. All tests were performed in triplicate.

2.6. Fabrication of the LFTS

The LFTS designed around N-CDs comprised five essential components: an absorbent pad, a test pad, a conjugation pad, a sample pad, and a PVC backing card (Fig. 1b). The sample pad, 1 cm in length, was crafted from glass fiber and positioned in the center of the LFTS to enable the bidirectional flow of the sample solution. The conjugation pad was strategically designed to connect with the sample pad and a nitrocellulose membrane on both sides. The N-CD solution was delicately sprayed onto the test pad, which was constructed using a nitrocellulose membrane in multiple small increments. Subsequently, the test pad was dried for 72 h at 55 °C. Absorbent pads were positioned on the outer edges of the strip to capture any excess solution. All these components were meticulously assembled in sequence on the PVC backing card. The assembled strips, each measuring 3.5 mm in width, were stored at room temperature for subsequent experiments. The outer packaging was manufactured using 3D printing technology.

2.7. Smartphone imaging

Standard solutions of AR18 with varying concentrations were added to the sample pad and allowed to stand for 2 minutes. During this time, the sample solution permeated into the trapping zone where N-CDs were added dropwise. Subsequently, the solution flowed towards the direction of absorbent pads. The entire detection process was performed at room temperature in a dark environment. Imaging was performed under UV lights. The LFTS was imaged using the rear camera of a smartphone. Relevant parameters for smartphone imaging were carefully recorded and adjusted to ensure the accuracy of the results and experimental repeatability. The color parameters of fluorescence images were analyzed through a smartphone app (called "Color Grab") and the corresponding RGB values were recorded for the quantitative analysis of AR18 (Fig. 1c).

2.8. Preparation of real samples

Carbonated beverages, milk and ice cream were chosen as the actual samples for this study. These products were purchased from a local supermarket in Ningbo. To prepare the samples for analysis, 30 mL of milk samples and carbonated beverages were filtered through a 0.22 μm microporous membrane. For ice cream, 1.0 g of ice cream was dissolved in 10 mL of warm water and the mixture was also filtered through a 0.22 μm polystyrene filter. After filtration, all crude products were centrifuged at 6000 rpm for 10 min and the supernatant was carefully collected and stored at 4 °C.

3. Results and discussion

3.1. Characterization of N-CDs

The morphology and size of N-CDs were thoroughly characterized using TEM, as shown in Fig. 2a. It clearly reveals the N-CDs as perfectly monodisperse, sphere-shaped particles with an average diameter of 5.2 ± 0.3 nm. Moreover, the high-resolution TEM (HRTEM) image reveals the distinct crystallinity of the N-CDs with well-resolved lattice fringes exhibiting a lattice spacing of 0.24 nm, originating from the (100) planes of graphite carbon.[19] The AFM image in Fig. 2b further confirms the monodispersity of the N-CDs with an approximate height of 1.2 nm. Meanwhile, the typical 22.1° and 44.7° diffraction peaks of amorphous carbon are observed in the XRD pattern (Fig. S1†), which can be associated with the (002) and (100) planes of graphite carbon, respectively.[20] The typical Raman spectrum of N-CDs (Fig. S2†) exhibits two peaks at 1381 cm^{-1} (D band) and 1569 cm^{-1} (G band), referring to the structural disorder within the sp^2 domain and the presence of the graphite phase, respectively.[21] The ratio of I_D/I_G = 0.85 implies a high degree of graphitization in N-CDs, aligning with their distinct crystallinity properties.

To gain insights into the chemical composition and surface functional groups of the N-CDs, FT-IR and XPS analyses were conducted. As depicted in Fig. 2c, FT-IR analysis revealed the characteristic peaks near 1040 cm^{-1} (C–N), 1175 cm^{-1} (C–O), and 1410 cm^{-1} (C–C) related to stretching vibrations.[22,23] The absorption peaks at 1630 cm^{-1} and 2960 cm^{-1} imply the presence of C=N/C=O and C–H bonds, while a broad absorption band in the range of 3100–3600 cm^{-1} suggests the stretching vibration of O–H/N–H, which shows the excellent water solubility of N-CDs.[24,25] Furthermore, the full XPS spectrum of N-CDs in Fig. 2d exhibits three prominent peaks at 285.1 eV (C 1s), 399.9 eV (N 1s) and 532.1 eV (O 1s), signifying that the N-CDs consist of C (64.43%), N (6.44%), and O (29.13%).[23] The high-resolution C 1s spectrum in Fig. 2e consists of three peaks at 284.2 eV, 285.9 eV, and 287.7 eV, which correspond to C=C/C–C, C–O/C–N, and C=N/C=O bonds, respectively.[22,26] The N 1s spectrum, as displayed in Fig. 2f, contains peaks at 399.2 eV and 401.3 eV, indicating the presence of C=N–C and N–H bonds.[27] The O 1s spectrum can be divided into two fitting bands, representing C=O (530.6 eV) and C–O (532.4 eV) bonds (Fig. S3†).[28] All of the above results support that N-CDs are rich in carbonization-related functional groups.

3.2. Optical properties of N-CDs

To obtain a comprehensive understanding of the optical properties of N-CDs, their UV-vis absorption and fluorescence spectra were recorded. As displayed in Fig. 2g, the UV-vis absorption spectrum shows two prominent absorption peaks at 268 nm and 348 nm, which originate from the π–π* transition of C=C bonds and the n–π* transition of C=O bonds, respectively.[29] The broad peak around 496 nm is associated with the n–π* transition of aromatic bands (C=N).[30] In addition, the fluorescence spectra of N-CDs indicate that they exhibit both the blue emission at 425 nm (under excitation at

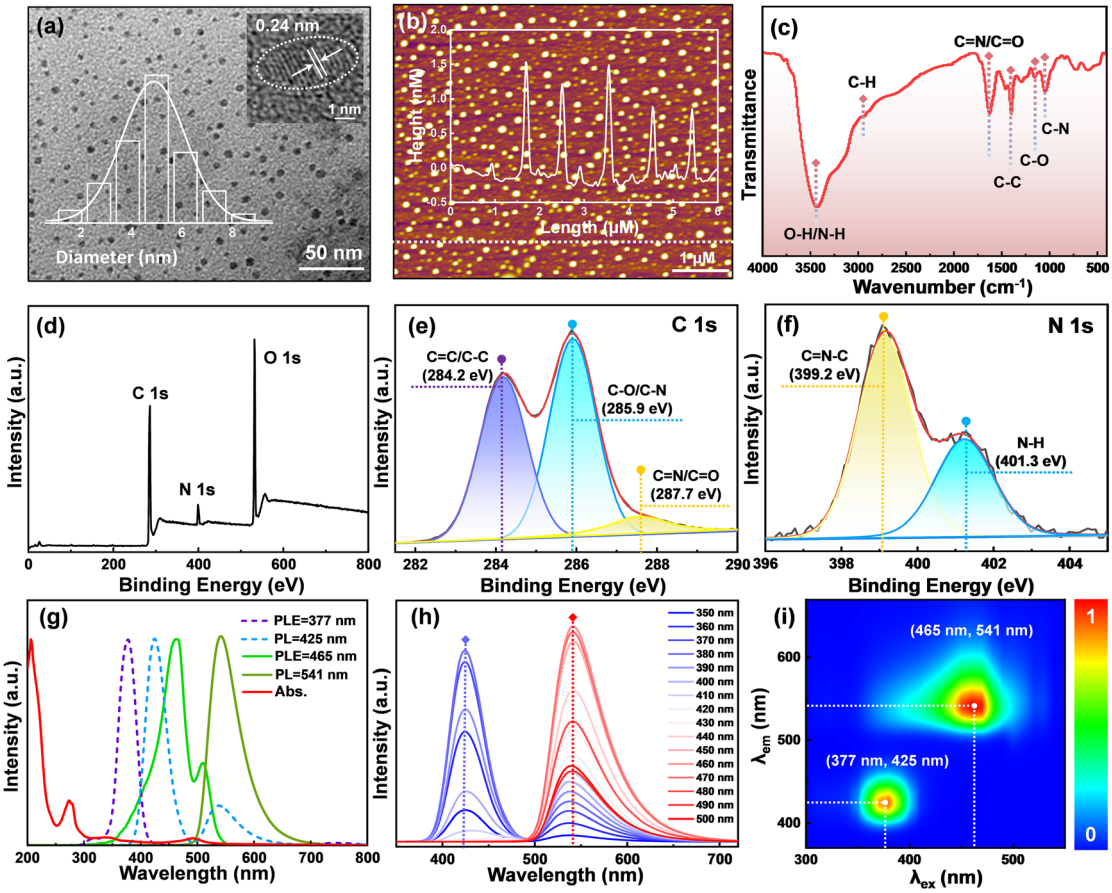

Fig. 2 (a) TEM image of N-CDs (the inset shows the size distribution and HR-TEM image of N-CDs). (b) AFM image of N-CDs. (c) FT-IR spectrum of N-CDs. (d) Full XPS spectrum of N-CDs. High-resolution XPS spectra of C 1s (e) and N 1s (f). (g) UV-vis absorption and fluorescence spectra of N-CDs. (h) Fluorescence spectra of N-CDs under different excitation wavelengths ranging from 350 to 500 nm. (i) Fluorescent matric scanning map of N-CDs.

377 nm) and the green emission at 541 nm (under excitation at 465 nm), revealing the bicentric-emissive characteristic of N-CDs. In addition, it is worth noting that N-CDs exhibit maximum QYs of 67.51% and 73% when excited at wavelengths of 377 nm and 465 nm, respectively (Fig. S4†). N-CDs exhibit excitation-independent properties when excited in the wavelength range from 350 nm to 500 nm, as shown in Fig. 2h. This consistency aligns with the separated bicentric emissions observed in the fluorescent matrix scanning map of N-CDs (Fig. 2i). The distinction between the two fluorescence areas, representing blue and green emission channels, lays a solid foundation for the determination based on the 3D fluorescence excitation–emission matrix of the luminophores of N-CDs.

For practical sensing applications of N-CDs, the fluorescence stability under varying time conditions and ionic strengths were studied. Fig. S5a† demonstrates that the fluorescence properties exhibit minimal changes across a range of NaCl concentrations (0–2 mol L^{-1}). Besides, the fluorescence behavior maintains excellent photostability during long-term storage (Fig. S5b†) and continuous irradiation under UV light (Fig. S5c†), suggesting a high resistance to photobleaching capability. These characteristics of excellent photostability and resistance to photobleaching in sunlight, at room temperature, and at different ionic strengths lay a strong foundation for the subsequent application of N-CDs in ratiometric fluorescence sensing.

3.3. Sensing mechanism of AR18

Due to the unique dual-emissive character and outstanding photostability exhibited by N-CDs, we conducted further investigations into their potential as fluorescence sensors. The impacts of 19 different interfering substances on the fluorescence of N-CDs were explored, as illustrated in Fig. S6.† It is worth noting that AR18 has the strongest fluorescence response among these interfering substances. Then the fluorescence response of N-CDs to AR18 was further elucidated through the following measurements. For pure N-CDs, bicentric emissions at around 425 nm and 541 nm are observed separately in Fig. 3a, which provide the appropriate dual-channel fluorescence signals for the application of N-CDs in ratiometric sensing. Upon introducing AR18, the emission at 541 underwent significant quenching due to the effective absorption of N-CD emission energy caused by AR18 (Fig. 3b), where a board UV-vis absorption of AR18 located at 520 nm has a large overlapping area with the

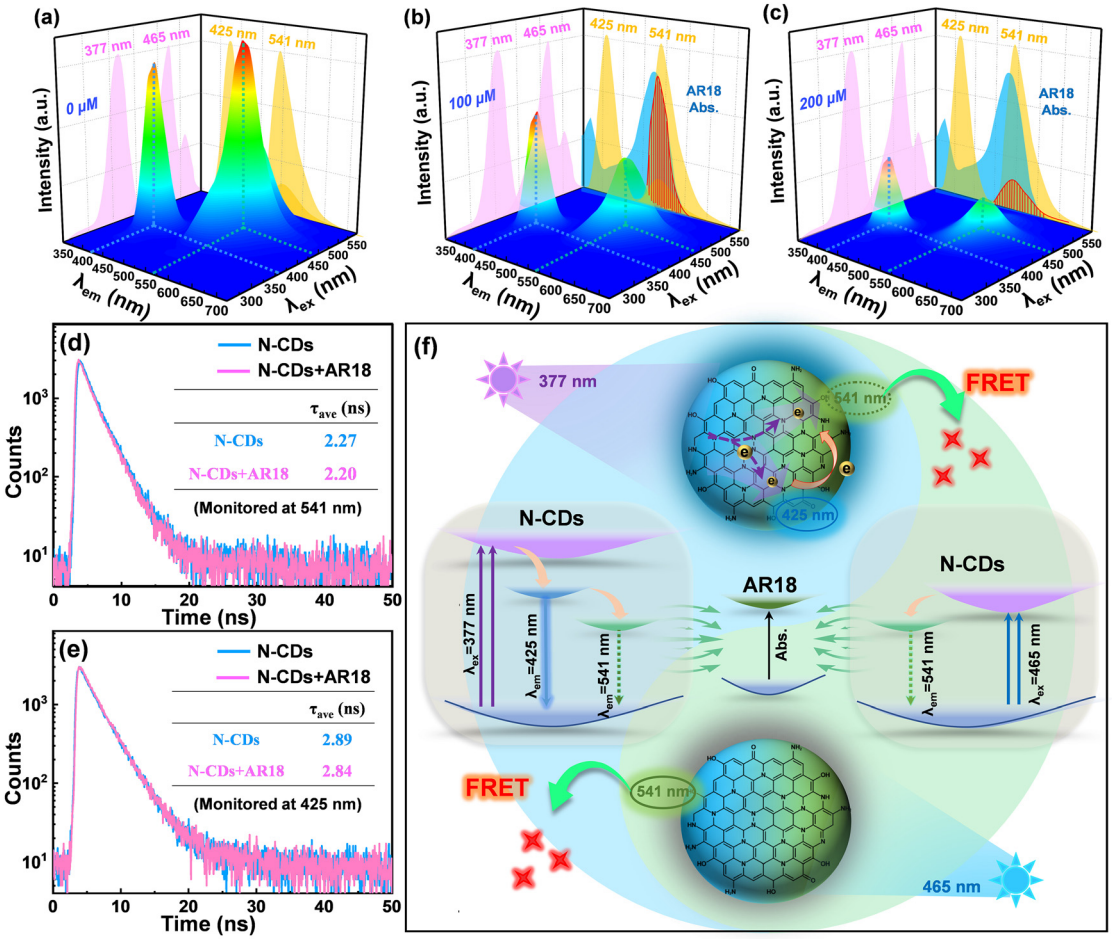

Fig. 3 (a–c) 3D fluorescent matric scanning maps of N-CDs with different concentrations of AR18. Fluorescence decay curves of N-CDs in the presence and absence of AR18 monitored at emission wavelengths of 541 nm (d) and 425 nm (e). (f) Schematic diagram of the fluorescence quenching mechanism of N-CDs.

green emission spectrum of N-CDs. As the dosage of AR18 increased, the green emission of N-CDs nearly completely quenched, while the blue emission remained perceptible, albeit with a slight reduction, showing a lower quenching efficiency compared to the green emission (Fig. 3c).

To gain a deeper understanding of the detection mechanism of the proposed probe, the dominating quenching of green emission was first examined. The UV-vis absorption spectra of N-CDs in the absence and presence of AR18 were recorded and are shown in Fig. S7.† The UV-vis absorption spectrum of N-CDs in the presence of AR18 showed a complete overlap with the theoretical one, implying that no complex is formed during the sensing process and ruling out the possibility of static quenching.[31,32] In addition, the relatively similar optical band gap of N-CDs (2.38 eV) compared to that of AR18 (2.21 eV) suggests the feasibility of competitive energy absorption between N-CDs and AR18. This implies that the green emission energy from N-CDs is sufficient to excite the AR18, as depicted in Fig. S8.†[33] Meanwhile, the zeta potential of N-CDs measured at 9.59 ± 0.80 mV and the negative charge of AR18 with a zeta potential of −16.82 ± 1.08 mV indicated the electrostatic attraction between them owing to their opposite polarity (Fig. S9†). The binding constant (K) of N-CDs and AR18, reflecting the interaction strength between the donor and acceptor, was calculated through the following Benesi–Hildebrand equation:[34]

$$\frac{1}{F_{541}-F_0}=\frac{1}{K(F_s-F_0)C}+\frac{1}{F_s-F_0} \quad (2)$$

where F_0, F_s and F_{541} are the fluorescence intensities of green emission at 541 nm of N-CDs without AR18, with a saturated analyte concentration of AR18 and with a certain dosage of AR18, respectively. C represents the concentration of the analyte. As shown in Fig. S10,† the calculated binding constant (K) between N-CDs and AR18 is remarkably high, measuring at 8.9×10^3 mol^{-1}. This value underscores a strong attraction between N-CDs and AR18, leading to a reduction in their separation distance. Recent reports suggest that the effective spectral overlap and close proximity of the donor and acceptor are conducive to FRET,[33,35] which shows that FRET is considered the predominant quenching mechanism responsible for the

attenuation of the green emission of N-CDs.[35] To further substantiate this assumption, the changes in the average fluorescence lifetime of N-CDs were explored, as shown in Fig. 3d. The decrease in the average fluorescence lifetime of N-CDs (from 2.27 to 2.20 ns) provides evidence of an energy transfer process transpiring between N-CDs and AR18.[36,37]

Regarding the modest quenching of the blue emission at 425 nm, it becomes evident that there is no significant overlap between the UV-vis absorption spectrum of AR18 and the blue emission spectrum of N-CDs, except for a slight overlap resulting from the trailing peak at 541 nm under shorter excitation wavelengths. The weak absorption of AR18 in relationship to the trailing emission in the blue channel disrupts the equilibrium of electron distribution, diminishing the electron density in blue channel of N-CDs under consistent excitation (at 377 nm). Consequently, this leads to a slight quenching of the blue emission at 425 nm. This explanation is supported convincingly by the slight reduction in the average fluorescence lifetimes of N-CDs at 425 nm (from 2.89 ns to 2.84 ns), as illustrated in Fig. 3e. Thus, the phenomenon of L-FRET, involving the selective absorption of green emission energy during the FRET process, results in varying degrees of quenching under two different excitations. This underscores the necessity of introducing ratiometric sensors based on a 3D fluorescence excitation–emission matrix, as depicted in Fig. 3f.

3.4. Determination of AR18 based on N-CDs

Leveraging the distinct reactivity of the two bimodal emissions, the N-CDs are harnessed to establish a ratiometric fluorescence sensing platform for the real-time monitoring AR18. As depicted in Fig. 4a, the fluorescence spectra of N-CDs under the optimal excitation wavelengths (425 nm and 541 nm) were derived from the normalized 3D fluorescent excitation–emission matrices of N-CDs at varying concentrations of AR18 (Fig. S11†). As the AR18 concentration increases, differential degrees of fluorescence quenching are manifested in the two monitored emissions, which are consistent with the dimming fluorescence under UV light (Fig. S12†). Notably, the emission at 541 nm experiences a more significant decrease compared to that at 425 nm. The intensity ratio between the two emissions (F_{541}/F_{425}) exhibit a negative correlation with the AR18 concentration over a range of 0.0539–300 μmol L^{-1}, as illustrated in Fig. 4b. In Fig. 4c, a calibration curve was fitted as $F_{541}/F_{425} = -0.008510C_{AR18} + 1.017$ in the linear range of 0.0539–30 μmol L^{-1}, with a coefficient of determination (R^2) of 0.997. Following the rule of $3\sigma/k$, the LOD was estimated as 53.9 nM, where σ represents the standard deviation of the blank solution and k signifies the slope of the fitting line.

Recognizing the potential complexity of real samples, we also studied the anti-interference properties of N-CDs by analyzing AR18 in the presence of each interferent, including K^+, Li^+, Ag^+, Ba^{2+}, Co^{2+}, Mg^{2+}, Cd^{2+}, Fe^{2+}, Ala, Asn, Cys, Glu, Pro, Ser, Cur, Tar, SY, and AMR (the concentration of each substance in a solution was 100 μM). As illustrated in Fig. 4d, the results reveal that the introduction of these interfering species has a negligible impact on fluorescence intensity of N-CDs@AR18. This observation underscores the exceptional selectivity and robust resistance to interference exhibited by N-CDs during the AR18 sensing process. Meanwhile, compared with the single-peak detection under different excitations, the LOD of 53.9 nM obtained from the ratiometric analysis is much lower than those of 102.7 nM and 67.1 nM (Fig. S13†). Furthermore, a comparative analysis with other previously reported fluorescent sensors is presented in Table S1.† The N-CD-based sensor consistently demonstrates superior detection performance, highlighted by its lower LOD.

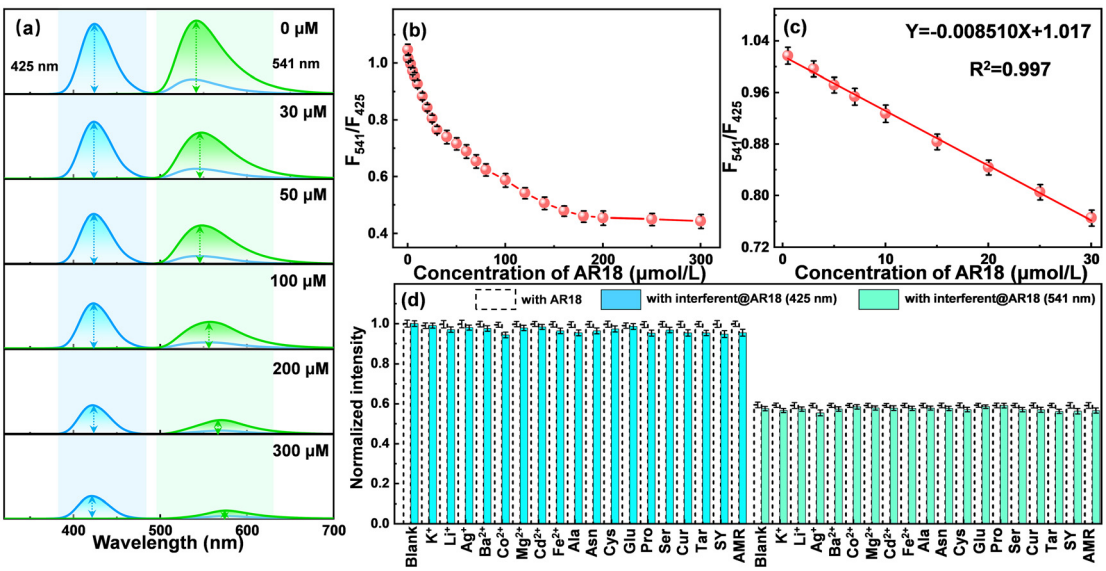

Fig. 4 (a) Fluorescence spectra of N-CDs with increasing concentrations of AR18 under excitation at 377 nm and 465 nm. (b) Relationship between the fluorescence intensity ratio (F_{541}/F_{425}) and the concentration of AR18. (c) Linear fitting between F_{541}/F_{425} and the concentration of AR18. (d) Effect of various metal ions and amino acids on the fluorescence intensity of N-CDs in the presence of AR18.

Therefore, the analytical method developed utilizing N-CDs represents a promising approach for the detection of AR18 with potential applications spanning various fields.

3.5. Portable sensing platform based on a LFTS

Addressing the limitations associated with real-time detections, such as the inaccuracies resulting from single changes in the fluorescence signals and the semi-quantitative nature of naked-eye monitoring, a portable fluorescence sensor based on a LFTS is proposed. As illustrated in Fig. 5a, the entire LFTS was designed to be bilaterally symmetrical, allowing for convenient monitoring of fluorescence responses under independent excitation sources (UV lamp with wavelengths of 365 nm and 470 nm, respectively). The N-CDs were preloaded into the capture buffer on both sides of the LFTS. Upon introduction of the AR18 standard solution to the sample pad, the capillary action drives the solution to both flanks, passing through the conjugation pad, and reaching the capture buffer. Valid results are discerned only when the capture buffer turns red under sunlight, signaling the presence of a standard solution (Fig. 5b). Under UV light, the green emission of N-CDs is substantially quenched due to the occurrence of L-FRET between N-CDs and AR18, while a slight reduction is observed in the blue emission under the 365 nm excitation. The fluorescence images were captured using a smartphone camera and analyzed through a smartphone application for precise intelligent detection.

After dropwise adding sample solutions, the flow of the fluid through the hydrophilic channels on LFTS is observed, as shown in Fig. S14,† further demonstrating the feasibility of LFTS application in real-time monitoring. Standard solutions of AR18 at various concentrations were tested using the proposed LFTS sensing platform and the typical results are shown in Fig. 5c. In contrast to the blue channel, which exhibits a marginal change in intensity, the green channel experiences a significant quenching effect with increasing AR18 concentration. The corresponding B values and G values of LFTS photographs were evaluated through a smartphone app and the relevant parameters were analyzed three times (Fig. 5d). As the analysis signal for AR18, the G/B value decreases with the addition of AR18. A linear equation was fitted to $G/B = -0.0143C_{AR18} + 0.992$ ($R^2 = 0.994$) over the concentration range of 0.0753–30 μM, with a LOD of 75.3 nM. These results underscore the significant potential of the LFTS sensing platform as a visual and user-friendly tool for AR18 detection.

3.6. Real sample assays

As a vital class of synthetic colorants, AR18 is extensively employed in food processing for its coloring properties. However, excessive accumulation of AR18 can disrupt the normal metabolic functions in the body. Consequently, the quantification of AR18 levels serves as a pivotal criterion for assessing food quality. To ascertain the suitability of the as-constructed LFTS sensing platform, we conducted experiments by spiking 100 μM of AR18 into three distinct real food samples (as illustrated in Fig. 6). The observed fluorescence changes strongly support the feasibility of detecting AR18 residues in food using our LFTS sensing platform. Furthermore,

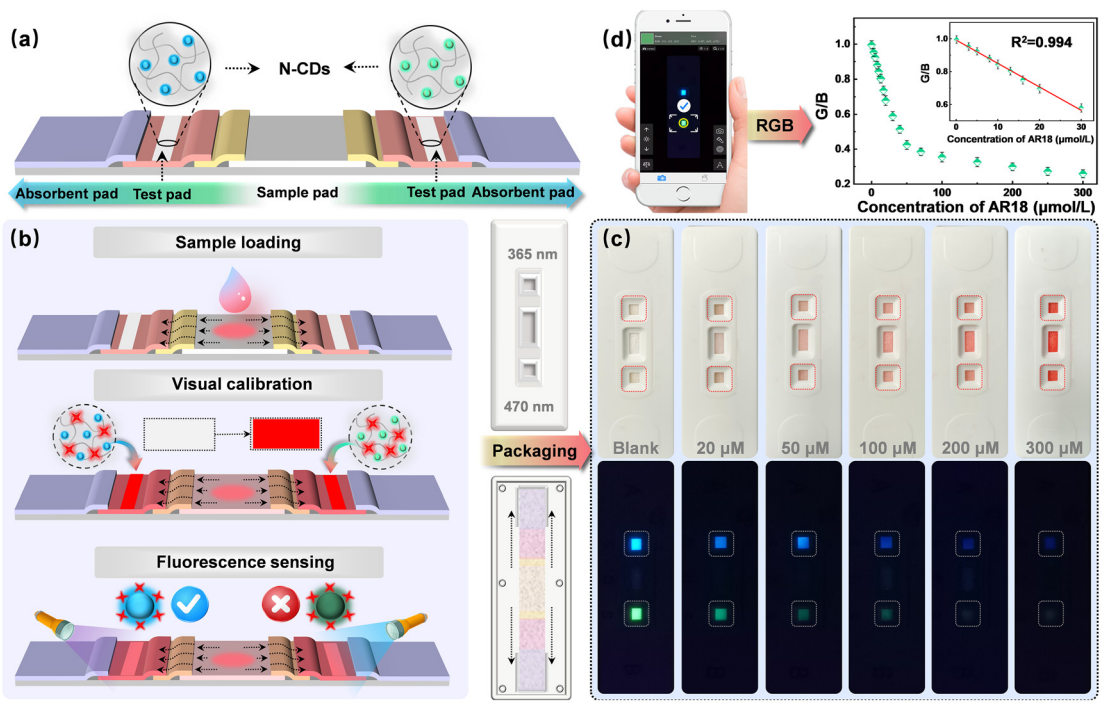

Fig. 5 (a) Hardware design of the LFTS. (b) Operation diagram illustrating the functioning of the LFTS. (c) Images of the sensing platform utilizing the LFTS with varying concentrations of AR18. (d) Correlation between the ratio value of G/B and the concentration of AR18.

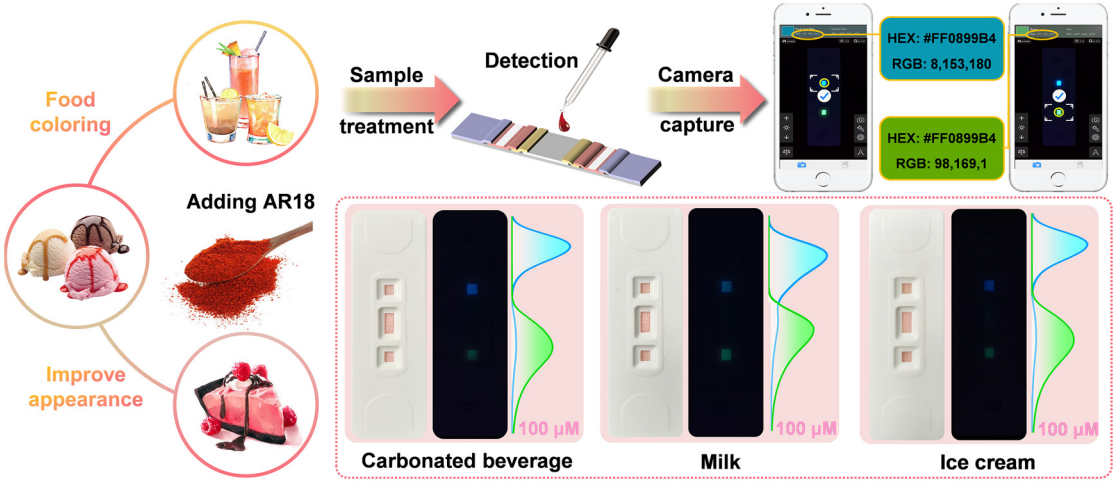

Fig. 6 Schematic diagram illustrating the detection of AR18 residues in real samples using the LFTS.

Table 1 Determinations of AR18 in real samples by fluorescence and HPLC

		Fluorescence		HPLC		
Sample	Spike (μM)	Detected (μM)	%Recovery (%RSD)	Detected (μM)	%Recovery (%RSD)	*t*-Test[a]
Carbonated beverages	10	10.08	100.8 (2.15)	10.06	100.6 (1.14)	0.86
	30	29.91	99.7 (1.13)	30.08	100.3 (0.55)	0.62
	50	50.31	100.6 (1.73)	50.14	100.3 (0.23)	0.71
Milk	10	10.14	101.4 (4.56)	9.98	99.8 (2.24)	0.52
	30	30.23	100.7 (0.34)	29.91	99.7 (1.78)	0.26
	50	50.37	100.6 (1.31)	50.26	100.5 (1.02)	0.78
Ice cream	10	10.10	101.0 (1.97)	10.04	100.4 (1.34)	0.57
	30	30.17	100.6 (0.73)	30.07	100.2 (0.52)	0.49
	50	50.18	100.3 (0.92)	49.92	99.8 (1.04)	0.43

[a] The critical *t*-value at the 95% confidence level is 2.78.

AR18 with concentrations of 10.0 μM, 30.0 μM and 50.0 μM were added into real samples of juice, milk and ice cream, respectively. These tests yielded highly satisfactory recoveries ranging from 99.7–101.4% with an RSD less than 4.56%, as summarized in Table 1. This demonstrates the exceptional accuracy of the LFTS sensing platform in determining AR18 levels in real food samples. To ensure the robustness of the as-constructed LFTS platform, we conducted *t*-tests when using HPLC as the reference method. The results showed a strong agreement between the two methods at a 95% confidence level. These findings underscore the stability of the LFTS platform in complex sample detection and highlight its immense potential for real-time monitoring of the AR18 content.

4. Conclusions

In summary, a novel strategy based on the fluorescence-bicentric N-CDs was developed for the straightforward and swift discrimination of AR18. The N-CDs derived from tris and resorcinol through the hydrothermal process exhibit dual-emission centers at 425 nm and 541 nm, corresponding to the excitation wavelengths of 377 nm and 465 nm, respectively. The introduction of AR18 results in varying degrees of fluorescence quenching in the two emission centers of N-CDs due to L-FRET, with the green emission experiencing a more substantial reduction than the blue emission. A ratiometric fluorescent probe for AR18 detection was constructed based on the 3D fluorescence maps with a low LOD of 53.9 nM within the linear detection range of 0.0539–30 μM. Furthermore, the integration of a LFTS and smartphone technology has significantly enhanced practicality, enabling simultaneous monitoring of two fluorescence signals and precise quantitative analysis of AR18, validating the application potential for AR18 identification. The constructed LFTS-based sensor possesses the merits of easy preparation, high sensitivity and ease of operation, offering a promising strategy for a convenient and on-site intelligent detection platform leveraging CDs.

Author contributions

D. C. and G. W. conceived the project. H. H., Z. C. and D. C. designed and performed the experiments. H. H., Z. C., T.

L., L. W., G. W. and D. C. performed the data analysis. H. H., Z. C., T. L., X. H., G. W. and D. C. contributed to the discussion. H. H., T. L., G. G., G. W. and D. C. prepared the figures. H. H., Z. C., T. L. and D. C. co-wrote the paper. All authors discussed the results and commented on the manuscript. The authors declare no competing financial interest.

Conflicts of interest

There are no conflicts of interest.

Acknowledgements

This work was supported by projects from the National Natural Science Foundation of China under Grant No. 61604084 and 62174093, the K. C. Wong Magna Fund in Ningbo University, the Ningbo Youth Science and Technology Innovation Leading Talent Project under Grant No. 2023QL006 and the Open Research Fund of China National Key Laboratory of Materials for Integrated Circuits (No. NKLJC-K2023-01).

References

1 M. Mohammadi, H. Ahangari, S. Mousazadeh, S. Hosseini and L. Dufossé, *Bioprocess Biosyst. Eng.*, 2022, **45**, 1–12.
2 S. Ghosh, T. Sarkar, A. Das and R. Chakraborty, *LWT – Food Sci. Technol.*, 2022, **153**, 112527.
3 P. Kolozof, A. Florou, K. Spyrou, J. Hrbac and M. Prodromidis, *Sens. Actuators, B*, 2020, **304**, 127268.
4 Y. Liu, M. Zan, L. Cao, J. Peng, P. Wang, X. Pang, Y. Zhang, L. Li, Q. Mei and W. Dong, *Microchem. J.*, 2022, **179**, 107453.
5 A. Ngo and D. Tischler, *Int. J. Environ.*, 2022, **19**, 4740.
6 E. Okeke, T. Ezeorba, C. Okoye, Y. Chen, G. Mao, W. Feng and X. Wu, *J. Food Compos. Anal.*, 2022, **114**, 104778.
7 T. Pham, V. Bui, T. Pham, T. Le, K. Nguyen, V. Bui and T. Nguyen, *Polymers*, 2021, **13**, 1536.
8 X. Li, Q. Zhang, K. Ma, H. Li and Z. Guo, *Food Chem.*, 2015, **182**, 316–326.
9 R. Zarrin and R. Sabzi, *J. Iran. Chem. Soc.*, 2022, **19**, 2973–2982.
10 Y. Chen, Y. Sun, X. Pang, R. Wang, G. Waterhouse and Z. Xu, *Biosens. Bioelectron.*, 2023, **241**, 115698.
11 M. Masar, P. Troska, J. Hradski and I. Talian, *Mikrochim. Acta*, 2020, **187**, 448.
12 J. Liu, Y. Zhan, B. Qiu, Z. Lin and L. Guo, *ACS Sens.*, 2023, **8**, 884–892.
13 L. Li, L. Yang, D. Lin, S. Xu, C. Mei, S. Yu and C. Jiang, *J. Hazard. Mater.*, 2023, **444**, 130403.
14 H. Ma, L. Guan, M. Chen, Y. Zhang, Y. Wu, Z. Liu, D. Wang, F. Wang and X. Li, *Chem. Eng. J.*, 2023, **453**, 139906.
15 Y. Hao, Y. Song, T. Li, Y. Tuo, M. Tian and F. Chai, *J. Environ. Chem. Eng.*, 2023, **11**, 109863.
16 Y. Cui, Z. Yang, L. Xiao, M. Yang, X. Gong, L. Liu, J. Han and Q. Hu, *J. Food Compos. Anal.*, 2023, **116**, 105053.
17 Y. Tu, Z. Liu, L. Jiang, Y. Xiang, F. Song, L. Meng, X. Ji and L. Yuan, *Dyes Pigm.*, 2022, **210**, 111024.
18 P. Keerthana, A. K. Das, M. Bharath, M. Ghosh and A. Varghese, *J. Environ. Chem. Eng.*, 2023, **11**, 109325.
19 C. Hsieh, C. Kao, Y. Gandomi, R. Juang, J. Change and R. Zhang, *J. Taiwan Inst. Chem. Eng.*, 2022, **133**, 104196.
20 Q. Hu, Y. Fang, Z. Guo, Z. Du, Z. Liu, Y. Yu, X. Tian and C. Tang, *Carbon*, 2022, **186**, 391–405.
21 H. Salee, A. Saud, N. Munira, P. Goh, A. Ismail, H. Siddiqui and S. Zaidi, *Nanomaterials*, 2022, **12**, 3519.
22 X. Luo, G. Huang, C. Bai, C. Wang, Y. Yu, Y. Tan, C. Tang, J. Kong, J. Huang and Z. Li, *J. Hazard. Mater.*, 2023, **443**, 130277.
23 Y. Hao, Z. Yang, W. Dong, Y. Liu, S. Song, Q. Hu, S. Shuang, C. Dong and X. Gong, *J. Hazard. Mater.*, 2022, **430**, 128393.
24 H. Li, T. Xu, Z. Zhang, J. Chen, M. She, Y. Ji, B. Zheng, Z. Yang, S. Zhang and J. Li, *Chem. Eng. J.*, 2023, **453**, 139722.
25 L. Zhu, D. Shen and K. Hong, *J. Colloid Interface Sci.*, 2022, **617**, 557–567.
26 H. Ma, L. Guan, M. Chen, Y. Zhang, Y. Wu, Z. Liu, D. Wang, F. Wang and X. Li, *Chem. Eng. J.*, 2023, **453**, 139906.
27 Z. Yang, T. T. Xu, S. B. Zhang, H. Li, Y. L. Ji, X. D. Jia and J. L. Li, *Nano Res.*, 2022, **1998**, 0124.
28 Z. Lu, S. Chen, M. Chen, H. Ma, T. Wang, T. Liu, J. Yin, M. Sun, C. Wu, G. Su, X. Dai, X. Wang, Y. Wang, H. Yin, X. Zhou, Y. Shen and H. Rao, *Chem. Eng. J.*, 2023, **454**, 140492.
29 S. Tang, Y. Wang, G. Guo, T. Li, H. Xing, H. Hu, X. Leng, C. Gu and D. Chen, *Sci. Total Environ.*, 2023, **872**, 162277.
30 J. Meng, H. Shen, L. Luo, J. Wang, Z. Xu and Y. Liu, *Sens. Actuators, B*, 2022, **365**, 131925.
31 A. Liu, H. Cai, Y. Zeng, Y. Chen, X. Yu, J. Song, P. Zeng, J. Qu, J. Guo and H. Li, *Anal. Chim. Acta*, 2022, **1225**, 340202.
32 Y. Zhu, Y. Lu, L. Shi and Y. Yang, *Microchem. J.*, 2020, **153**, 104517.
33 K. Yang, P. Jia, J. Hou, S. Zhao and L. Wang, *Food Chem.*, 2022, **396**, 133693.
34 S. Liao, Z. Ding, S. Wang, F. Tan, Y. Ge, Y. Cui, N. Tan and H. Wang, *Spectrochim. Acta, Part A*, 2020, **259**, 119897.
35 J. Yang, Y. Huang, H. Cui, L. Li and Y. Ding, *J. Fluoresc.*, 2022, **32**, 1815–1823.
36 M. Li, C. Liu, L. Qi and H. Liu, *Nano Mater.*, 2022, **5**, 5425–5438.
37 L. Yang, J. Wen, K. Li, L. Liu and W. Wang, *Sens. Actuators, B*, 2021, **333**, 129557.